

Exciton Polaritons Reveal “Hidden” Populations in Functionalized Pentacene Films


Published as part of *The Journal of Physical Chemistry virtual special issue “W. E. Moerner Festschrift”*.

Jonathan D. B. Van Schenck, Winston T. Goldthwaite, Richard Puro, John E. Anthony, and Oksana Ostroverkhova*

 Cite This: *J. Phys. Chem. C* 2021, 125, 27381–27393

 Read Online

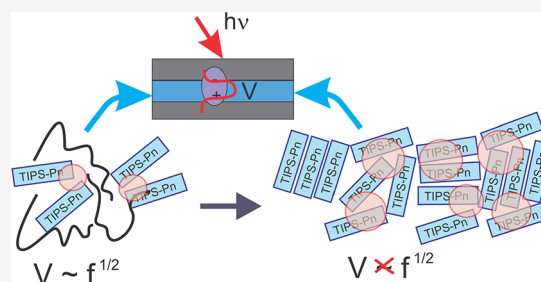
ACCESS |

 Metrics & More

 Article Recommendations

 Supporting Information

ABSTRACT: We present a systematic investigation of strong exciton–photon coupling in functionalized pentacene (TIPS-Pn)-based films in all-metal cavities, depending on molecular concentration and film morphology. Rabi splittings of up to 270 meV are observed, with the highest values achieved in pristine amorphous TIPS-Pn films. The exciton–photon interaction strength for the lowest-energy (0–0) excited state scaled with the square root of the molecular density, which was independent of whether the long-range molecular order were present in films. The molecular populations in the disordered regions of the films coupled to the cavity most strongly in all films, including pristine crystalline films. Such populations, with molecular configurations favoring interaction with the cavity electromagnetic field, were not readily identifiable in optical absorption spectra of bare (i.e., not coupled to the cavity) films, which highlights the capability of polariton spectroscopy to reveal these molecular ensembles, which are “hidden” in polycrystalline films. The linear scaling of the exciton–photon interaction strength with the square root of the oscillator strengths was observed in dilute TIPS-Pn:PMMA films but not in pristine TIPS-Pn films, either amorphous or crystalline. In particular, in pristine films, the exciton–photon interaction strength for the vibronic (0– m , $m > 0$) excitons was higher than expected based on the oscillator strengths extracted from the optical spectra of bare films, which was attributed to enhanced exciton delocalization facilitated by the 2D brickwork motif of TIPS-Pn. Similar observations were made in functionalized anthradithiophene (diF TES-ADT) films (also exhibiting a 2D brickwork packing motif) but not in functionalized tetracene (TIPS-Tc) films, which suggests that the underlying mechanisms rely on short-range intermolecular interactions determined by the molecular packing motif and resulting nanomorphology.



1. INTRODUCTION

Organic (opto)electronic and photonic materials have attracted attention due to their low cost, solution processability, and tunable properties.¹ A broad range of (opto)electronic and photonic applications, including organic light-emitting diodes (OLEDs), photovoltaics (OPVs), field-effect transistors (OFETs), sensors, photorefractive three-dimensional displays, and lasers, have been demonstrated, and many of them have been commercialized.^{1,2} One of the areas that has experienced recent dramatic growth is research into strong coupling between organic molecules and resonant structures, such as microcavities,^{3,4} plasmonic nanostructures,⁵ or hyperbolic metamaterials,⁶ and associated physics and applications of this phenomenon. The complexity of interactions involved in the strong coupling and how they translate into properties of light–matter hybrid states (polaritons) have inspired theoretical effort^{7–10} and enabled experimental demonstrations of Bose–Einstein condensation and associated exciting phenom-

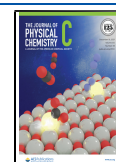
ena including polaritonic lasing,^{11–13} nonlinear amplification,¹⁴ and superfluidity.¹⁵

Additionally, it has been of considerable interest to understand how strong coupling, and the resulting light–matter hybrid polariton states, may contribute to the performance of organic (opto)electronic devices.^{16–20} For example, exciton polaritons in organic photodiodes incorporated into microcavities enhanced the device responsivity by extending the photodiode sensitivity to wavelengths beyond those achievable in the absence of strong coupling.¹⁷ In a planar OPV incorporated in a resonant cavity, strong coupling-modified optical absorption enabled reduction in the losses.²⁰

Received: September 19, 2021

Revised: November 23, 2021

Published: December 7, 2021



In perylene diimide field-effect transistors on plasmonic nanostructures, an order of magnitude enhancement in charge carrier mobility was observed and attributed to an enhanced carrier delocalization promoted by hybrid states.²¹ On the other hand, charge carrier mobilities in organic transistors based on donor–acceptor copolymers or phthalocyanines incorporated in resonant cavities were similar to those in control devices without the cavity structures.^{22,23} Therefore, more work is needed to understand the polariton properties in organic semiconductors, their contribution to characteristics of organic (opto)electronic devices, and underlying mechanisms that determine (opto)electronic properties.

Over the past decade, strong coupling has been demonstrated in a variety of organic materials, expanding the library of polaritonic materials well beyond traditional organic polaritonic systems involving J-aggregates dispersed in polymer films or gels.²⁴ This includes materials that have been previously explored for (opto)electronic applications. Examples are photorefractive glasses such as a dicyanomethylene-dihydrofuran derivative (exhibiting ultrastrong coupling with Rabi splitting of >1 eV),²⁵ OLED and OPV materials such as 4,4'-cyclohexylidenebis[*N,N*-bis(4-methylphenyl)-benzenamine] (TAPC)²⁶ and phthalocyanines,¹⁷ and OFET materials such as derivatives of acenes (e.g., anthracene (Ac), tetracene (Tc), pentacene (Pn))^{27–31} and of anthra-dithiophenes (ADTs).³² In addition to their attractive electronic properties, acenes and ADTs have served as model systems for photophysical studies on all levels, from single molecules incorporated in solids,^{33–37} which began from seminal demonstration of optical detection of single Pn molecules dispersed in a *p*-terphenyl crystal,³³ to molecular crystals.^{38–41} Many of these derivatives (including Tc, Pn, and ADT) exhibit singlet fission (SF), the process of creating two triplet (T_1) excitons upon excitation of a singlet (S_1) state ($S_0 + S_1 \rightarrow TT \rightarrow T_1 + T_1$, where TT is a correlated triplet pair that serves as a precursor to the free triplets), which has generated a considerable amount of attention due to its potential to enhance the efficiency of organic solar cells.⁴²

One representative benchmark electronic and SF material of this class is Pn functionalized with triisopropylsilylethynyl (TIPS) side groups (TIPS-Pn).⁴³ In field-effect transistors (FETs), TIPS-Pn exhibits hole mobilities of >1 cm²/(V s) and up to 11 cm²/(V s), depending on the crystal polymorph and/or film crystallinity and morphology.^{1,44} These are among the highest mobilities in solution-processable OFETs, which has motivated research into mechanisms responsible for its enhanced electronic characteristics and into structure–property relationships over the past 20 years.^{39,44–49} In terms of photophysics, TIPS-Pn films exhibit ultrafast (<100 fs) SF, depending on film morphology,^{50–53} and this process in TIPS-Pn has been extensively studied from the fundamental photophysics standpoint^{53–57} and toward applications in SF-based photovoltaics.⁵⁸ Although photophysical and electronic properties of TIPS-Pn have been extensively studied, exploration of properties of polaritons in TIPS-Pn is at its inception,^{31,59} and an understanding of how the underlying photophysics of TIPS-Pn and specifics of TIPS-Pn film morphology determine these properties has not yet been developed. Such an understanding, however, would be important for designing materials for next-generation organic electronic devices utilizing properties of polaritons, which motivates our present study.

In this paper, we investigate strong coupling of excited states in TIPS-Pn-based films of varying TIPS-Pn concentration and morphology to cavity photons in all-metal microcavities. Inspired by the capability of single molecule spectroscopy to reveal “hidden” molecular populations in ensembles masked by ensemble averaging,⁶⁰ we demonstrate how polariton spectroscopy identifies “hidden” populations that couple to the microcavity. The existence of these populations is not readily observed with optical spectroscopy of bare films, yet they are important for polaritonic devices. We observe preferential cavity coupling of TIPS-Pn molecules in the amorphous phase over the crystalline phase in heterogeneous (mixed-phase) films and in the defect-rich regions in the crystalline phase, whose importance for the SF process has been recently demonstrated.⁵⁰ We establish that the scaling of the exciton–photon interaction strength for the vibrationless (0–0) excited state with the square root of the molecular density is independent of film crystallinity and morphology. In contrast, the scaling of the interaction strength for the vibronic excitons with the square root of the oscillator strengths depends on the molecular density and breaks down for highly concentrated TIPS-Pn films, which we relate to nanomorphology and associated with it the degree of vibronic exciton delocalization.

2. METHODS

2.1. Sample Preparation. The microcavities were fabricated by using the following procedure: first, a 45 nm silver (Ag) layer was deposited onto a glass (BK7) substrate via thermal evaporation, then a film was spin-cast to form the active layer with a thickness of ~100–200 nm (to create resonant $\lambda/2$ cavities), and finally another 45 nm Ag layer was evaporated on top of the film to finish the cavity. This top Ag layer was masked to only cover a portion of the total substrate, allowing part of the active layer of the same sample to be measured in both “coupled” (that is, contained in the cavity) and “uncoupled” (that is, with no top mirror) states. Regions without (with) the top Ag layer are termed “bare film” (“cavity”).

Various types of TIPS-Pn films were used as the active layer in the microcavities as schematically shown in Figure 1, classified as “blends” and “pristine”. In the case of blends, TIPS-Pn molecules were embedded in a polymer matrix of poly(methyl methacrylate) (PMMA) at several TIPS-Pn concentrations. For this, TIPS-Pn and PMMA were dissolved in toluene at varying relative concentrations to control the relative density of TIPS-Pn molecules in the resulting film such that the average TIPS-Pn molecular spacing was between $d = 1$ nm and $d = 2$ nm. Calculations of relative concentrations and the resulting average molecular spacings can be found in the Supporting Information.^{32,61} For example, concentrations of 13 mM TIPS-Pn with 40 mg/mL PMMA and 53 mM TIPS-Pn with 20 mg/mL PMMA were used to achieve an average TIPS-Pn molecular spacing of $d = 2$ nm and $d = 1$ nm, respectively. Films were deposited at spin-casting speeds between 800 and 3000 rpm. These films are termed $F_d^{(B)}$, where the superscript *B* indicates the film is a blend and the subscript denotes the average TIPS-Pn molecular spacing in nanometers (e.g., $F_2^{(B)}$ and $F_1^{(B)}$ in Figure 1).

The “pristine” TIPS-Pn films contained only TIPS-Pn molecules (no PMMA) and were deposited by using a 50 mM solution of TIPS-Pn in toluene via spin-casting. To improve the film quality, the Ag surface was treated with a 30 mM solution of pentafluorobenzenethiol (PFBT) in ethanol

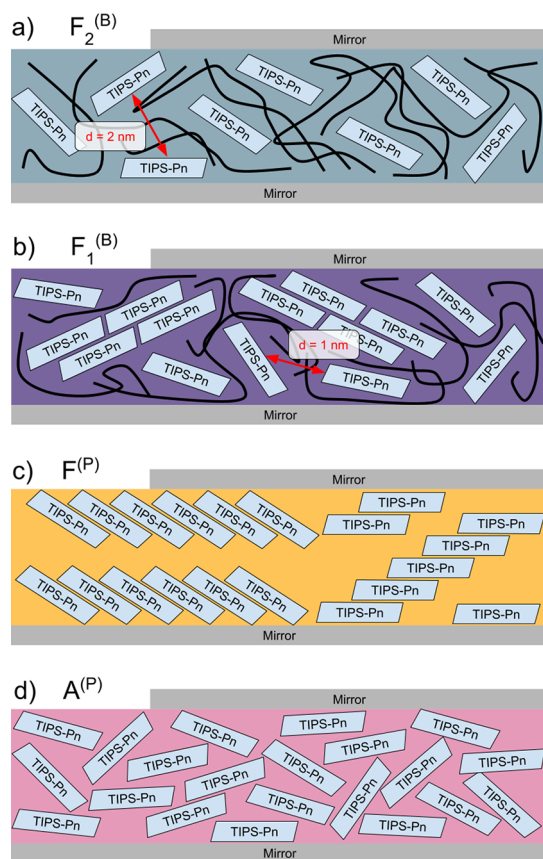


Figure 1. Schematic representations of the morphology in four film types embedded in an optical cavity. (a) Film $F_2^{(B)}$ has TIPS-Pn embedded in a PMMA matrix with average molecular spacing (d) of 2 nm. (b) Film $F_1^{(B)}$ has both amorphous phase TIPS-Pn and crystallites (ordered aggregates) embedded in a PMMA matrix. The average molecular spacing (d) is 1 nm. (c) Film $F^{(P)}$ is a polycrystalline film with the dominant orientation (00 l) (for $l = 1, 2, 3$), with the long c -axis of the crystal in the substrate normal direction which is represented on the left of the cavity, with the minor population with (011) orientation schematically represented on the right. (d) Film $A^{(P)}$ is an annealed pristine film where TIPS-Pn molecules are in the amorphous phase.

(as described in previous publications^{32,62}). The pristine TIPS-Pn films obtained by using this deposition method were polycrystalline as confirmed by X-ray diffraction (XRD), and they exhibited (00 l) ($l = 1, 2, 3$) and (011) orientations of TIPS-Pn (Figure S1).⁴⁹ These films are referred to as $F^{(P)}$, where the superscript P indicates the film is pristine.

To force polycrystalline films into an amorphous state, thermal annealing was employed. Details of this process can be found in the Supporting Information and Figure S2. Briefly, after spin-casting, films were placed on a hot plate and held at 250 °C for 20 s, allowing the film to fully convert into an amorphous phase as confirmed by the XRD (Figure S1a). These films are termed $A^{(P)}$, where the A indicates that the film has been annealed and is amorphous.

2.2. Optical Characterization. The solution absorption spectrum was measured in a 30 μ M solution of TIPS-Pn in toluene placed in a 1 cm fused silica cuvette by using a tungsten lamp (Ocean Optics LS-1) and a fiber-coupled spectrometer (Ocean Optics USB2000). The spectrum was fit by using a vibronic progression model^{38,68} (eq S16) as described in section S5 of the Supporting Information.

The microcavities were characterized by using angle-resolved reflectance on a custom-built optical assembly. White light from a fiber-coupled tungsten filament source (Ocean Optics LS-1) was passed through a linear polarizer to select either s - or p -polarizations before being focused onto the sample at angles of incidence ranging from 15° to 80° in steps of 5°. Reflected light was then collected and analyzed with an Ocean Optics USB2000 spectrometer. The absorbance for each bare film was measured by using the reflectance of that film at low angle of incidence (15°). The bare film and the microcavity data were modeled as described in the Supporting Information (eqs S17 and S18, respectively).

The photoluminescence (PL) spectra of the bare films were measured by exciting the samples with a continuous wave 532 nm frequency-doubled Nd:YVO₄ laser (Verdi-5, Coherent, Inc.) and collecting the emitted light with a calibrated Ocean Optics USB2000-FLG spectrometer.³⁸ The PL spectra of select films are shown in Figure S10. The PL lifetimes were measured by using 532 nm pulsed excitation from a frequency-doubled Nd:YAG laser (NE Fianium-1060), and the emitted photons were collected by using a PDM Series single-photon avalanche photodiode (SPAD) and a time-correlated single-photon counting card (TimeHarp 200, Picoquant, Inc.). The measurements were limited by an instrument response function to a resolution of 380 ps.

2.3. Numerical Analysis. The center energies of the cavity reflection resonances were modeled by using a coupled oscillators model for polaritons³² as described in section S8 of the Supporting Information (eqs S19 and S20). Briefly, the Hamiltonian (eq S19) containing angle-dependent cavity photon energy $E_{ph}(\theta)$ (eq S20), up to four excited state energies $E_X^{(0i)}$, depending on the film, and interaction energies V_{0i} was numerically diagonalized at each angle of incidence to obtain the polariton branch energies. These were then compared to the center energies $E_n(\theta)$ (obtained from fits to the angle-dependent reflectance from the cavities with eq S18) in a nonlinear least-squares optimization to determine the interaction strengths V_{0m} .

The exciton–photon interaction strength was considered to be in the following form:⁶³

$$V = \frac{\hbar\Omega}{2} = \mu \sqrt{\frac{N_0 \hbar\omega}{2\epsilon \mathcal{V}_{\text{mode}}}} \quad (1)$$

where V is the interaction energy, $\hbar\Omega$ is the Rabi splitting, μ is the transition dipole moment of the molecules coupled to the cavity, N_0 is the number of cavity-coupled molecules inside the photon mode volume $\mathcal{V}_{\text{mode}}$, $\hbar\omega$ is the photon energy, and ϵ is the dielectric constant of the cavity-filling material. Of particular relevance here is that this predicts $V \propto \mu \propto \sqrt{f}$, where f is the oscillator strength of molecule's absorptive transition.

As a result, the interaction strengths $2V_{0m}$ (Rabi splitting) for each film were modeled with a linear fit:³²

$$2V_{0m} = A \sqrt{f_{0m}/f_{00}} + B \quad (2)$$

where f_{0m} is the oscillator strength of the m th transition, extracted from fits to the spectra of bare film. Although eq 1 predicts that the interaction strength scales with the transition dipole moment (equivalently the root of the oscillator strength), it has been shown³² that this proportionality is not always accurate for molecular aggregates due to intermolecular

effects not accounted for by eq 1. To address this particular observation that for some films, the observed $2V_{0m}$ versus f_{0m} dependence is considerably weaker than a proportional model ($B = 0$) would suggest; the linear model (eq 2) is applied in two forms. For TIPS-Pn:PMMA films, B is fixed at zero reducing the model to the expected proportionality. For pristine TIPS-Pn films, A is fixed at zero reducing the model to a constant fit. The parameter values are given in Table S7.

Finally, the lowest-energy (0–0) exciton–photon interaction energies $2V_{00}$ were also fit by using a proportional model with the square root of the molecular density, estimated via the molecular volume \mathcal{V} :

$$2V_{00} = C \sqrt{\frac{1}{\mathcal{V}}} \quad (3)$$

where C is a proportionality constant; fit parameters are given in Table S8.

Section S1 in the Supporting Information provides a detailed description of how these volumes were calculated for each film.

3. RESULTS

3.1. Optical Properties of Bare Films. Figure 2 shows absorption spectra of various types of bare TIPS-Pn:PMMA

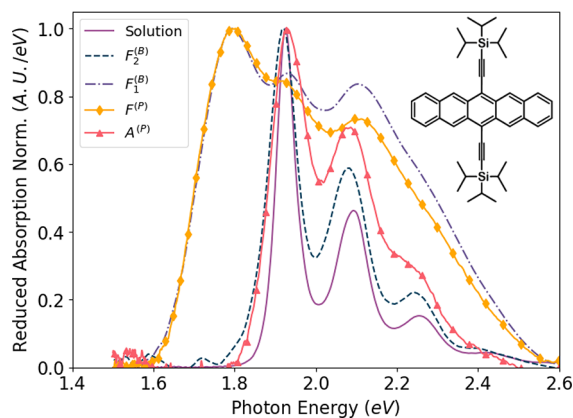


Figure 2. Reduced absorption (normalized to the 0–0 peak height) from four TIPS-Pn films deposited onto a silver substrate: film $F_2^{(B)}$ (dashed), film $F_1^{(B)}$ (dash-dotted), film $F^{(P)}$ (diamonds), and film $A^{(P)}$ (triangles). The reduced absorption spectrum from TIPS-Pn in dilute (30 μM) solution in toluene is also shown (solid) for comparison. The $F_2^{(B)}$ and $A^{(P)}$ films show an amorphous phase response, with a 0–0 transition energy of ~ 1.9 eV, which is similar to that of dilute solution. Both the $F_1^{(B)}$ and $F^{(P)}$ films show a crystalline phase response, with a 0–0 transition energy of ~ 1.8 eV. The inset shows the molecular structure of TIPS-Pn.

and pristine TIPS-Pn films used in this study, schematically depicted in Figure 1, as well as that of TIPS-Pn in dilute toluene solution. The spectrum in dilute solution shows the characteristic vibronic progression expected for noninteracting TIPS-Pn molecules (Figure S4), with the 0–0 energy of 1.926 eV and a Huang–Rhys (HR) factor of $S = 0.74$ due to coupling to an effective C–C stretching mode at 0.164 eV. The HWHM of the 0–0 peak σ_{00} was only 25 meV though the progressive broadening $\Delta\sigma$ was large (0.67), indicating that the electronic excitation is coupled to a distribution of C–C stretching modes, possibly in combination with C–H and CCC bending modes,^{64–67} centered on 0.164 eV (Table 1).⁶⁸

The dilute TIPS-Pn:PMMA blend $F_2^{(B)}$ exhibited spectra similar to that of dilute solution, which were also modeled with a vibronic progression (Figure S5). The 0–0 energy in $F_2^{(B)}$ is at 1.916 eV (10 meV lower than in solution, due to differences in the dielectric environment), and the vibronic progression shows coupling to an effective C–C stretching mode at 0.162 eV with the HR factor of $S = 0.72$. The 0–0 HWHM σ_{00} is 36 meV (slightly larger than that in solution), but the progressive broadening $\Delta\sigma$ is only 0.31, less than half of that in solution. This is indicative of the PMMA environment imposing restrictions on the molecular vibrational degrees of freedom, decreasing the width of the distribution of the vibrational modes that the electronic excitation can couple to (decreasing $\Delta\sigma$) while also presenting a more inhomogeneous local environment for the molecules (increasing σ_{00}).

In contrast, spectra of the more concentrated TIPS-Pn:PMMA blend $F_1^{(B)}$ featured an ~ 0.14 eV (~ 50 nm) red-shift of the 0–0 energy (1.78 eV) and significant peak broadening—features similar to those in pristine polycrystalline TIPS-Pn films $F^{(P)}$ (Figure 2, Figures S7 and S8). These spectral changes are due to intermolecular interactions, and they are consistent with previous studies of TIPS-Pn films and single crystals.^{48,52,56,69,70} For example, the 0–0 red-shifts of 45–70 nm in polycrystalline TIPS-Pn films have been previously observed depending on morphology,⁴⁸ and the large 0–0 solution–crystal red-shifts in TIPS-Pn crystals were attributed to efficient mixing of the Frenkel and charge transfer (CT) states.⁷⁰ Furthermore, GW/BSE calculations confirmed that the lowest-energy exciton in crystalline TIPS-Pn possesses a charge transfer (CT) character and is delocalized over ~ 3 nm in the a – b plane of the crystal.⁵⁶ The development of this phase (which will be termed “crystalline”, as the emergence of the low-energy 1.78 eV peak in the optical absorption spectra strongly correlates with the emergence of crystalline-phase molecular packing⁵⁷ and crystalline structure detected by the XRD, Figure S1b) in concentrated blends, with the pronounced effects of TIPS-Pn intermolecular interactions on the optical absorption spectra, can be seen in the spectra of blends $F_d^{(B)}$ with $1 < d < 2$. For example, in the optical spectrum of a TIPS-Pn:PMMA film $F_{1.3}^{(B)}$ (Figure S6), both the crystalline and amorphous (that is, having optical absorption spectra similar to those of dilute blends and amorphous films $A^{(P)}$, Figure 2) contributions could be identified, constituting 64% and 36%, respectively, of the total signal. Similar concentration-dependent evolution of spectral features has also been observed in films of anthradithiophene (ADT) derivatives such as a benchmark organic semiconductor material diF TES-ADT (TES = triethylsilyl ethynyl),^{38,61} blended with PMMA at various concentrations. The diF TES-ADT exhibits trends in polariton behavior similar to those in TIPS-Pn, which will be discussed in section 4 to highlight that the observations presented here for TIPS-Pn represent a general trend for a particular class of functionalized acenes and ADTs.

The pristine TIPS-Pn amorphous films $A^{(P)}$ had absorption spectra with features considerably more similar to those of dilute TIPS-Pn:PMMA blends (such as $F_2^{(B)}$) than to those in the polycrystalline films $F^{(P)}$, in agreement with previous work (Figure S9).^{48,53,57} In particular, the 0– m peak energies in the S_0 – S_1 manifold were close to those in dilute blends and solutions. However, the 0– m peak ratios and the peak widths were different from those in dilute blends (Table 1), which suggests that intermolecular interactions are not negligible in

Table 1. Excited-State Properties in Solution and Bare Films and Polariton Properties in Cavities^a

system	E_X^{00} (bare) (eV)	E_V (eV)	S	σ_{00} (meV)	$\Delta\sigma$	E_X^{00} (cav) (eV)	$2V_{00}$ (meV)
solution	1.93	0.16	0.72	25	0.67		
$F_2^{(B)}$	1.92	0.16	0.74	36	0.31	1.91	85
$F_1^{(B)}$	1.79*			74*		1.91	228
$A^{(P)}$	1.93	0.15	0.85	44	0.33	1.93	253
$F^{(P)}$	1.77*			65*		1.73	210

^aThe 0–0 excited-state energies (E_X^{00} (bare)), vibrational energy (E_V), Huang–Rhys parameter (S), HWHM of the 0–0 line (σ_{00}), and line broadening ($\Delta\sigma$) obtained from fits to the absorption spectra of bare films and solution with a vibronic progression with Lorentzian line shapes (eq S16). *In $F_1^{(B)}$ and $F^{(P)}$, data were fitted with a set of four Gaussian functions in eq S17; the 0–0 transition energy and a standard deviation are included in the table for these films; full list of parameter values can be found in Tables S3 and S4. Also included are the 0–0 transition energy (E_X^{00} (cav)) for the population that couples to the cavity and interaction strengths ($2V_{00}$) associated with the s-polarized polaritons in representative cavities containing $F_2^{(B)}$, $F_1^{(B)}$, $F^{(P)}$, and $A^{(P)}$ films extracted from fits utilizing a model of eq S19. A full list of cavity parameter values is given in Table S6.

these films⁷¹ even though the lowest-energy exciton does not show spectral signatures of Frenkel–CT mixing and delocalization in these amorphous films $A^{(P)}$. We note that, in contrast to dilute blends and amorphous films, the 0– m transitions in crystalline films are not a simple vibronic progression due to a complicated mixture of various states of Frenkel and CT nature contributing to each peak.^{38,69,70} Nevertheless, in the following discussions of the crystalline films (e.g., $F_1^{(B)}$ and $F^{(P)}$), the notation “0– m ” is used to differentiate between different peaks contributing to the absorption spectra in the 1.8–2.4 eV energy region for easier comparison to other films.

PL measurements revealed additional insights into the photophysics of films under study. In particular, in TIPS-Pn:PMMA blends $F_2^{(B)}$ and $F_{1,3}^{(B)}$, and in pristine amorphous films $A^{(P)}$, the PL spectra were similar (Figure S10), exhibiting the 0–0 energy close to that in dilute solutions and a vibronic progression. However, the PL yield was considerably different, with the dilute blend $F_2^{(B)}$ exhibiting about a factor of ~ 20 stronger PL than the amorphous pristine film $A^{(P)}$ under the same excitation conditions. Additionally, considerable shortening of the PL lifetimes was observed as the TIPS-Pn concentration increased (Figure S11 and Table S5), with the biexponential dynamics in all films as compared to the monoexponential 13.8 ns decay in solution. For example, in the amorphous pristine film $A^{(P)}$, PL lifetimes of 0.6 and 3.0 ns were obtained as compared to 1.4 and 5.2 ns in the dilute TIPS-Pn:PMMA blend $F_2^{(B)}$, which indicates higher availability of nonradiative decay pathways in pristine films. The PL yield dramatically decreased with the appearance of the 1.78 eV exciton in the optical absorption spectra, and so the PL in pristine crystalline films $F^{(P)}$ was more than 2 orders of magnitude weaker than that in dilute blends $F_2^{(B)}$. The concentration-dependent evolution of PL properties is due to a combination of enhanced exciton diffusion, enabling nonradiative decay pathways, and an onset of singlet fission, which is more efficient in more concentrated and, especially, crystalline phases of TIPS-Pn.⁵² Therefore, the PL emission in our TIPS-Pn films largely originates from molecules that are in configurations not conducive to singlet fission, either due to a large spatial separation or due to unfavorable molecular orientations.

3.2. Optical Properties of Films in Microcavities.

Figures 3, 4, and 5 illustrate optical properties of films discussed above placed in microcavities. All films reveal formation of light–matter hybrid states (exciton polaritons), exhibiting dispersive characteristics observed in the angle-

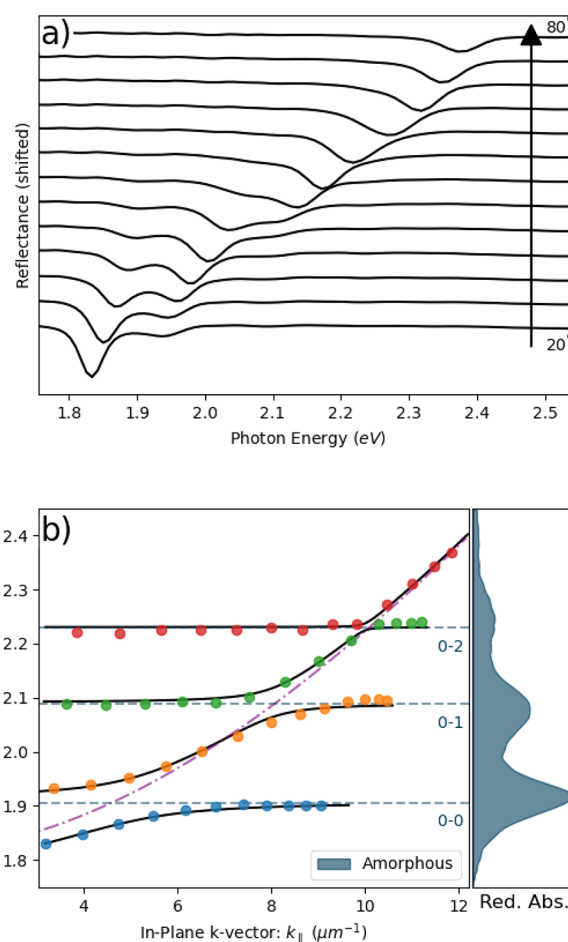


Figure 3. (a) Reflectance from a cavity containing the film $F_2^{(B)}$ at angles of incidence ranging from 20° to 80° . (b) Dispersion plot of the polariton energies extracted from the reflectance. Dots show the experimentally extracted energies, the dash-dotted line shows the photon energy, the dashed line shows the excited-state energies for the “amorphous” phase, and solid black lines show fits according to the coupled oscillator model. On the right side of (b), the reduced absorption from the corresponding bare film is included for comparison.

dependent reflectance spectra (e.g., Figures 3a and 4a). The exciton–photon coupling strengths were obtained by using a coupled oscillator model as described in section 2.3 and our previous publication.³² The interaction strengths for the lowest-energy, vibrationless excited singlet state (termed “0–0 exciton” in all discussions below for notation simplicity) that

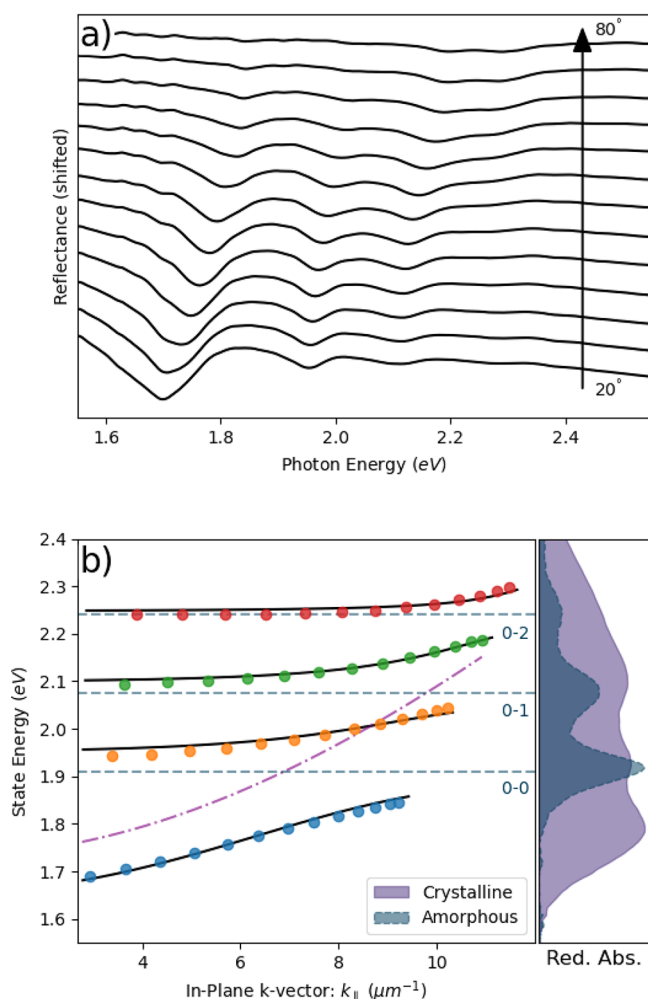


Figure 4. (a) Reflectance from a cavity containing the $F_1^{(B)}$ film at angles of incidence ranging from 20° to 80° . (b) Dispersion plot of the polariton energies extracted from the reflectance. Dots show the experimentally extracted state energy, the dashed-dotted line shows the photon energy, the dashed line shows the excited-state energies for amorphous phase, and solid black lines show fits according to the coupled oscillator model. Adjacent to (b) is the reduced absorption from the corresponding film (solid line) which shows a crystalline phase response and the reduced absorption for a $F_2^{(B)}$ film with an amorphous phase response (dashed line) shown for comparison. Notice that the photon is coupled to the amorphous phase in the cavity, despite the absorption spectrum showing a predominately crystalline phase.

couples to the cavity photon obtained in all films are summarized in Tables 1 and S6, featuring the Rabi splitting values ($\hbar\Omega_{00} = 2V_{00}$) between 85 meV in the dilute TIPS-Pn:PMMA films $F_2^{(B)}$ and 253 meV in pristine amorphous TIPS-Pn films $A^{(P)}$ for s-polarized light. In each film, coupling of at least three molecular states (corresponding to 0– m transitions for $m = 0, 1, 2$) to the cavity photon was observed for s-polarized light (Figures 3b, 4b, and 5), whereas in p-polarization, coupling to only two molecular states (corresponding to 0– m transitions for $m = 0, 1$) could be resolved in most films. Interaction strengths for each transition for all cavities studied are summarized in Table S6.

The microcavity containing a dilute TIPS-Pn:PMMA film $F_2^{(B)}$ exhibited coupling strengths for the 0– m ($m = 0, 1, 2$) transitions of 85, 62, and 16 meV (in the s-polarization, Table

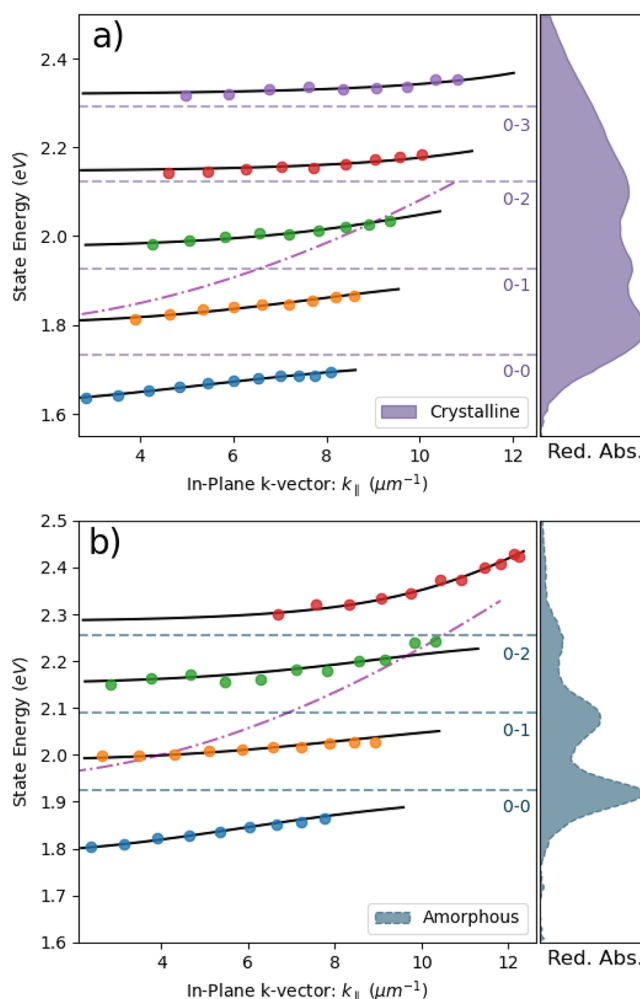


Figure 5. Comparison of the s-polarized polariton dispersions in pristine TIPS-Pn cavities: (a) crystalline film ($F^{(P)}$) cavity with the adjacent reduced absorption of the bare film for comparison and (b) amorphous film ($A^{(P)}$) cavity of comparable to (a) thickness with the adjacent reduced absorption for the bare film shown. For both plots, dots show the experimentally extracted state energies, the dashed-dotted line shows the photon energy, the dashed lines show the exciton energies, and the solid lines show the fits according to the coupled oscillator model. Fit parameter values are given in Table 1 and Table S6.

S6) which scaled well with the square root of the oscillator strength (f_{0m}), obtained from fits of the corresponding bare film absorption spectrum with a vibronic progression (Figure S5), predicted by eq 1 (Figure 6a). The more concentrated blends TIPS-Pn:PMMA $F_{1,3}^{(B)}$ and $F_1^{(B)}$ reveal interesting behavior. Although the absorption spectrum in bare films of this type was dominated by the spectral features of the crystalline phase (Figure 2 and Figure S6), the coupling to the cavity occurred for excited states corresponding to those of amorphous phase rather than to those of crystalline phase (Figure 4b and Figure S12). Figure 4b illustrates this preferential coupling for the $F_1^{(B)}$ by showing absorption spectra of the bare film $F_1^{(B)}$ (dominated by those of the crystalline phase) and of bare film $F_2^{(B)}$ (dominated by those of the amorphous phase) side by side with the dispersion characteristics of various polariton branches in $F_1^{(B)}$ cavities. The obtained interaction strengths $2V_{0m}$ (228, 182, and 121 meV for 0–0, 0–1, and 0–2 transitions, respectively, in s-

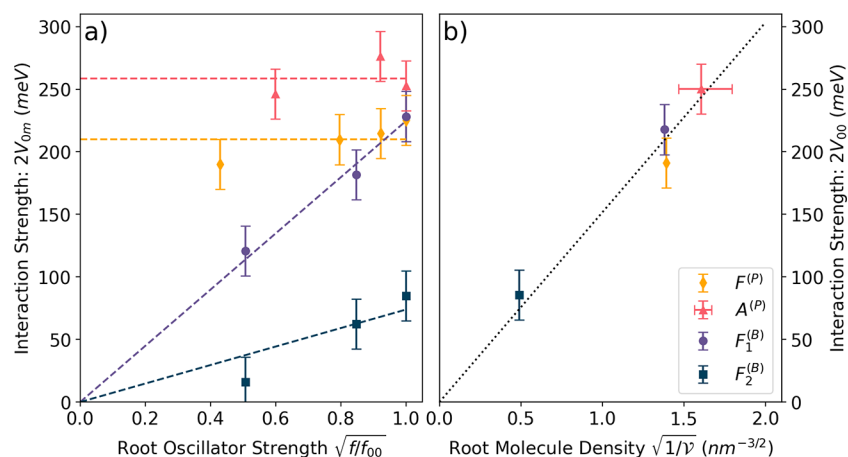


Figure 6. (a) Comparison of the interaction strengths ($2V_{0m}$, $m = 0, 1, 2, 3$) for s-polarized polaritons in each cavity ($F_2^{(B)}$, $F_1^{(B)}$, $F^{(P)}$, and $A^{(P)}$) as plotted against the square root of the oscillator strength f_{0m} (relative to that of the 0–0 transition) for the associated transition. For amorphous films $F_2^{(B)}$ and $A^{(P)}$, the oscillator strength is taken as the Franck–Condon (FC) coefficient ($e^{-S^2}/m!$ where the HR factor S , Table 1). For $F_1^{(B)}$, the oscillator strengths for $F_2^{(B)}$ are used. The dashed lines for each set of data represent either a proportional fit or a constant fit (eq 2) to highlight the deviation from a proportional model. Fit parameters are listed in Table S7. (b) Comparison of the 0–0 interaction strength ($2V_{00}$), averaged for s- and p-polarized polaritons in each cavity type, plotted against the square root of the effective molecular density $N_{\text{tot}} = 1/\mathcal{V}$, where \mathcal{V} is the molecular volume. The dotted line represents a proportional fit based on eq 3. Vertical error bars were estimated at 20 meV based on the coupled oscillators model fit. Fit parameters are listed in Table S8.

polarization) scale well with the square root of oscillator strength f_{0m} (Figure 6a) for the amorphous phase. Additionally, the value of $2V_{00} = 228$ meV for $F_1^{(B)}$ is about 2.7 times larger than $2V_{00} = 85$ meV in $F_2^{(B)}$ (as expected from the increased molecular density N_{tot} in $F_1^{(B)}$ over $F_2^{(B)}$ and $2V_{00} \propto \sqrt{N_{\text{tot}}}$ scaling) by a factor of $\sqrt{(2/1)^3} \approx 2.8$. This is intriguing since the amorphous phase in the concentrated TIPS-Pn:PMMA blend $F_1^{(B)}$ was not readily apparent in the absorption spectra of the corresponding bare films (Figure 2).

In contrast to concentrated TIPS-Pn:PMMA blends such as $F_1^{(B)}$, in pristine amorphous films $A^{(P)}$ the cavity photon coupled to the expected excited states, corresponding to 0– m ($m = 0, 1, 2$) molecular transitions characteristic of the amorphous phase (Figure 5b). Furthermore, the polycrystalline films $F^{(P)}$ exhibited cavity coupling of excited states characteristic of the crystalline phase (Figure 5a), in spite of the similarity in the bare film optical absorption properties for $F_1^{(B)}$ and $F^{(P)}$ (Figure 2). The interaction strength $2V_{00}$ for the amorphous films $A^{(P)}$ of 253 meV was higher than 210 meV for polycrystalline films $F^{(P)}$, as expected from increased molecular density in amorphous films (see section S1 and Figure S3 in the Supporting Information). However, an interesting observation common for amorphous $A^{(P)}$ and polycrystalline $F^{(P)}$ films is that the coupling strength of the oscillators corresponding to 0– m transitions to the cavity does not scale with the square root of the oscillator strength (extracted from fits to the absorption spectra of bare films), which is in stark contrast to observations in TIPS-Pn:PMMA blends $F_1^{(B)}$ and $F_2^{(B)}$ (Figure 6a). This behavior has been previously observed in highly concentrated diF TES-ADT:PMMA blends in similar cavities,³² data for which are included for comparison in Figure S13a, as discussed in the next section.

4. DISCUSSION

The exciton–photon coupling in various film types (Figure 1) reveals an interesting picture of how the evolving film density and morphology modify the cavity-coupling characteristics in

TIPS-Pn-based films. In particular, there are two unexpected observations (Figure 6):

- (1) In concentrated TIPS-Pn:PMMA blends (such as $F_1^{(B)}$ or $F_1^{(B)}$) with both the amorphous and crystalline phases present, the amorphous phase exhibits the strong exciton–photon coupling (Figure 4 and Figure S12), whereas the crystalline phase does not, even though the optical absorption spectra are strongly dominated by those of the crystalline phase (Figure 2, Figures S6 and S7).
- (2) The expected scaling of the interaction strength $2V_{0m}$ with the square root of the oscillator strength f_{0m} breaks down in pristine films, both polycrystalline $F^{(P)}$ and amorphous $A^{(P)}$, even though it works well for TIPS-Pn:PMMA blends.

Next, we discuss the possible underlying mechanisms behind these observations.

4.1. Effect of Morphology: Preferential Cavity Coupling to Amorphous Phases. Figure 6b illustrates that the coupling between the cavity photon and the lowest-energy excited state (0–0) described by $2V_{00}$ scales as expected with the square root of the overall molecular density N_{tot} ($2V_{00} \propto \sqrt{N_{\text{tot}}} \propto \sqrt{1/\mathcal{V}}$, where \mathcal{V} is the molecular volume, section S1 in the Supporting Information), in spite of differences in the lowest-energy excited-state properties in the crystalline and amorphous films seen from Figure 2.

To understand this behavior, we follow Spano’s estimate in ref 7 (adapted to molecules under study) that the Rabi splitting in the lowest polariton branch of ~ 235 meV could be achieved by cavity coupling of $N_0 = 2.5 \times 10^6$ molecules (obtained by using the cavity photon energy $\hbar\omega$ of 2 eV, transition dipole moment μ of 4 D (see section S9 for the estimate), dielectric constant ϵ of 3, and photon mode volume $\mathcal{V}_{\text{mode}}$ of $1 \mu\text{m}^3$ in eq 1), which translates into the molecular density $N = N_0/\mathcal{V}_{\text{mode}}$ of $2.5 \times 10^{18} \text{cm}^{-3}$. As the Rabi splitting in this estimate is in the range of the interaction strengths $2V_{00}$ obtained in pristine TIPS-Pn films (e.g., $2V_{00} = 210\text{--}250$ meV

in s-polarization, Figure 6a), we compare the estimated $N = 2.5 \times 10^{18} \text{ cm}^{-3}$ with the total molecular density N_{tot} of the order of 10^{21} cm^{-3} in our pristine films (calculated as described in section 2.3, Figure 6b). The comparison suggests that only a small fraction ($\alpha = N/N_{\text{tot}} = 2.5 \times 10^{-3}$) of all molecules couple to the cavity, whereas the rest of the molecules contribute to the reservoir of dark exciton states.^{8,9,72} Because the $2V_{00}$ coupling energy scales as expected with the overall molecular density N_{tot} (Figure 6b), so that the 0–0 excited state in more dilute films exhibits proportionally lower coupling strengths $2V_{00}$, a similar fraction ($\alpha = 2.5 \times 10^{-3}$) of all molecules participate in coupling of the 0–0 transition to the cavity in all films, regardless of the molecular concentration. We note that the transition dipole moment μ in highly concentrated films would be expected to slightly deviate from the value estimated above for the isolated molecules due to intermolecular interactions;^{38,57,61} however, no contribution of this deviation to the concentration-dependent coupling strengths $2V_{00}$ was apparent.

In terms of existing models, for example by using Spano's approach in ref 8, the observed scaling of $2V_{00}$ with the molecular density in Figure 6b would be presented as $2V_{00} \propto \sqrt{N_{\text{tot}}}$, where $N_{\text{tot}} = (1/\alpha)(1/V_{\text{mode}}) \times N_{\text{agg}} \times N_{\text{M}}$. Here, N_{agg} is the number of aggregates resonantly coupled to the cavity and N_{M} is the number of molecules in the aggregate.⁸ The data in Figure 6b for the 0–0 exciton–photon coupling would, for example, be consistent with the N_{agg} linearly increasing with the increased molecular concentration, as it evolves from blend $F_2^{(B)}$ to pristine films $F^{(P)}$ and $A^{(P)}$, while N_{M} remains unchanged (Figure 7a).

Although the optical absorption spectra and properties of the 0–0 exciton in particular exhibit pronounced differences among films under study, depending on the molecular concentration and morphology (Figure 1 for TIPS-Pn and Figure 1 of ref 32 for diF TES-ADT), the preserved scaling of $2V_{00}$ with the square root of the overall molecular density N_{tot} (Figure 6b) suggests that a small population of molecules (a fraction α of the N_{tot}) with similar properties, such as molecular arrangements that maximize interactions with the cavity electric field, couple to the cavity in all films, regardless of the macroscopic film morphology and crystallinity. We hypothesize that this population does not rely on long-range crystalline order, but draws from the disordered regions, with properties dominated by those of molecules themselves and nearest-neighbor interactions, instead.

To confirm the molecular, as opposed to crystalline, origin of the cavity-coupled population, we calculated the oscillator strengths for the S_0 – S_1 transition for isolated R-Pn and diF R-ADT molecules (where R is a side group, see section S9 and Table S9)³⁸ using density functional theory (DFT). The square root of the ratio of the DFT-calculated diF R-ADT and R-Pn oscillator strengths $f_{S_0-S_1}$ of 1.23 ± 0.02 , obtained without taking account any intermolecular interactions, is comparable to the ratio of the slopes (1.4 ± 0.1) of the proportional relationship ($2V_{00} \propto \sqrt{N_{\text{tot}}}$) obtained from linear fits of the data in Figure S13b and Figure 6b for diF TES-ADT and TIPS-Pn (239 ± 9 and $166 \pm 8 \text{ meV/nm}^{-3/2}$, Table S8).

These estimates are also consistent with our previous observations of $2V_{00} = 271 \pm 11 \text{ meV}$ (where the $2V_{00}$ value is the average over p- and s-polarizations over three cavities of various detunings) obtained in pristine amorphous films of TIPS-Tc in similar all-metal cavities (e.g., Figure S14).³⁰ The

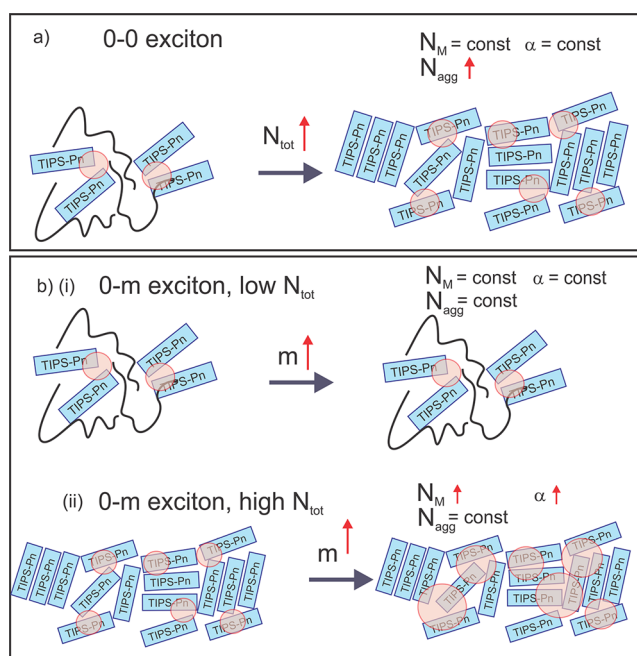


Figure 7. (a) Schematics of changes in 0–0 exciton–cavity photon coupling with increasing molecular density N_{tot} : change in the number of aggregates coupled to the cavity N_{agg} without affecting the delocalization (the number of molecules in the aggregate, N_{M}). Cavity-coupled regions (fraction α of the overall molecular density N_{tot}) are represented by red circles. “0–0 exciton” = lowest-energy (vibrationless) excited singlet state. (b) Schematics of changes in 0– m exciton–cavity photon coupling with increasing m at low (i) and high (ii) molecular density N_{tot} . “0– m exciton” = excited state corresponding to the 0– m vibronic transition. At low molecular density, N_{agg} and N_{M} remain the same for the vibronic excitons as for vibrationless (0–0) exciton. At high molecular density, the interaction strength $2V_{0m}$ increases with m due to an increased exciton delocalization (increased N_{M}) of the vibronic excitons, which could be represented by an increase in the fraction α of the molecules coupled to the cavity.

R-Tc molecule has a DFT-calculated S_0 – S_1 oscillator strength $f_{S_0-S_1}$ in between those for R-Pn and diF R-ADT (Table S9), and the obtained coupling strength $2V_{00}$ of $\sim 270 \text{ meV}$ in pristine TIPS-Tc films is as expected, in between the polarization-averaged $2V_{00}$ coupling strengths for pristine TIPS-Pn (~ 190 – 240 meV for $F^{(P)}$ and $A^{(P)}$) and high-concentration crystalline diF TES-ADT:PMMA films ($\sim 320 \text{ meV}$ in P_{agg} ³²). Therefore, the 0–0 exciton–photon coupling is a primarily molecular effect.

The cavity-coupling disordered populations are the dominant type of population for dilute TIPS-Pn:PMMA blends $F_2^{(B)}$ and amorphous films $A^{(P)}$, but they represent a minor, “hidden” population in the crystalline films $F_1^{(B)}$ and $F^{(P)}$. In particular, our procedure for deconvolution of optical absorption spectra, which separates the contributions of the crystalline and amorphous phases to the overall spectra (e.g., Figure S6 and Table S2 for $F_{1.3}^{(B)}$), did not detect the presence of the amorphous phase in the concentrated TIPS-Pn:PMMA blend $F_1^{(B)}$ (Figure S7 and Table S3). Yet, the polariton properties indicate that this is the population which couples to the cavity most efficiently in $F_1^{(B)}$ (Figure 4). Similar observations in diF TES-ADT:PMMA films of various diF TES-ADT concentrations³² suggest that such preferential cavity coupling to disordered populations is not unique for

TIPS-Pn and could be a general trend for a variety of acene and ADT materials and beyond.⁷³

Finally, in pristine crystalline films $F^{(P)}$, the coupled oscillators model yields a 0–0 exciton energy of 1.73 eV (Table 1 and Figure 5a), which is 40 meV lower than 1.77 eV for the 0–0 peak extracted from the fits of the absorption spectra from the bare films (Table 1 and Figure S9). In keeping with observations of preferential coupling to amorphous phases in mixed-phase films, we hypothesize that this low-energy excited-state population draws from defect states in the crystallites or at their edges, with short-range interactions close to those of the disordered populations in amorphous films. Interestingly, a distinct molecular population with the exciton energy centered at 1.72 eV has been recently identified in TIPS-Pn microcrystals by using ultrafast microscopy,⁵⁰ and this population (termed “nonequilibrium” in ref 50) formed predominantly on morphological defect-rich sites within the crystallite and at crystallite edges. Because of the closely matched energies of the excited singlet state of the “nonequilibrium” population and of the entangled triplet pair (TT) state (precursor state to the free triplet states in the SF process), as well as the presence of strong CT character, which is important for the SF, the existence of this population had a considerable impact on the TT dynamics. Our observations would be consistent with the preferential cavity coupling to molecules in this “nonequilibrium” low-energy population, and our findings may present an opportunity to manipulate the (TT) state dynamics by cavity coupling in polycrystalline TIPS-Pn cavities.

Extending this logic toward cavity coupling of single TIPS-Pn crystals with a (001) orientation similar to that dominant in the polycrystalline films (Figure S1), but having fewer defects as compared to films, one would expect a lower $2V_{00}$ coupling strength in crystals because of their lower density of disordered molecular populations. Although this hypothesis remains to be proven in single crystals of TIPS-Pn, our explorations of solution-grown diF TES-ADT crystals in all-metal cavities, which exhibit the same two-dimensional brickwork packing motif and the (00*l*) (*l* = 1–4) preferential orientation on the substrate as TIPS-Pn,^{38,62} support this hypothesis. In particular, $2V_{00}$ of 120 meV was obtained from analysis of multiple diF TES-ADT crystals for light polarized along the long axis of the crystal,⁷⁴ which is lower than 300–340 meV, depending on polarization, obtained in high-concentration polycrystalline diF TES-ADT:PMMA blends P_{agg} .³² However, further investigation is necessary to understand the cavity coupling in films versus single crystals depending on crystal orientations and crystal structure.

4.2. Effect of Exciton Properties: Enhanced Cavity Coupling of Delocalized Vibronic Excitons. Figure 6a illustrates that the TIPS-Pn:PMMA cavities $F_1^{(B)}$ and $F_2^{(B)}$ follow the expected scaling relationship of the coupling strengths V_{0m} for the 0–*m* exciton transitions with the square root of the 0–*m* oscillator strength ($2V_{0m} \propto \sqrt{f_{0m}}$), whereas the pristine cavities (both amorphous $A^{(P)}$ and crystalline $F^{(P)}$) do not. This encompasses two interesting observations: (i) it is apparent from the optical absorption and PL spectra of bare films that the properties of the excited states in the amorphous and crystalline phases are considerably different, yet the scaling behavior of $2V_{0m}$ with the oscillator strength is similar in $A^{(P)}$ and $F^{(P)}$. Moreover, optical spectra of bare amorphous pristine films $A^{(P)}$ are considerably more similar to those of the dilute

blends $F_2^{(B)}$ than to those of the pristine crystalline films $F^{(P)}$ (Figure 2). It is curious, then, that the $2V_{0m}$ scaling with f_{0m} in amorphous pristine films $A^{(P)}$ is pronouncedly different from that in the $F_2^{(B)}$ films. What the excited states in pristine films $A^{(P)}$ and $F^{(P)}$ do have in common is that they must experience short-ranged intermolecular interactions of the neighboring molecules with π – π overlap. For example, both the amorphous and crystalline phases exhibit singlet fission⁵² mediated by intermolecular interactions, though the process is more efficient in the crystalline phase. (ii) When comparing the lowest-energy (0–0) exciton coupling strengths $2V_{00}$ for films of varying molecular density, TIPS-Pn films follow the scaling relationship ($2V_{00} \propto \sqrt{N_{\text{tot}}} \propto \sqrt{1/V}$) up to and including the pristine films (see Figure 6b and Table S8). This indicates that the interaction strength for the lowest-energy exciton in the pristine TIPS-Pn films scales as expected, while the vibronic (0–*m*, *m* > 0) excitons have a higher than expected interaction strengths (i.e., than what would be predicted by the $2V_{0m} \propto \sqrt{f_{0m}}$ relationship).

What remains to be understood, then, is why the vibronic excitons in the pristine TIPS-Pn cavities have a higher interaction strength than what is expected from the analysis of the oscillator strengths in the optical absorption of bare films. Applying Spano’s model used above,^{7,8} one possible explanation is that the full scaling relationship $2V_{0m} \propto \sqrt{f_{0m}N}$ is still applicable but that the value of *N* represents an *effective* number of coupled molecules per mode volume which is larger for the higher-energy excitons (compensating for a lower oscillator strength). In particular, if these excitons are delocalized over a larger number of molecules than the lowest-energy (0–0) exciton, as it has been predicted by GW/BSE,⁵⁶ then a higher number of molecules would be within the photon’s mode volume, increasing the effective molecular density that couples to the cavity photon. With the N_{agg} and N_{M} notations introduced above,⁸ the scenario for the data in pristine TIPS-Pn films in Figure 6a would be represented as $2V_{0m} \propto \sqrt{f_{0m}N}$, where $N = \alpha N_{\text{tot}} = (1/V_{\text{mode}})N_{\text{agg}} \times N_{\text{M}}$ with the N_{agg} determined by the molecular density N_{tot} (which is a constant for a film with a given molecular concentration) and N_{M} increasing with *m* for 0–*m* vibronic excitons in pristine TIPS-Pn cavities due to enhanced exciton delocalization (Figure 7b(ii)), which is equivalent of increasing a fraction of the molecules α that participate in the coupling to the cavity. This delocalization could either arise directly from larger coherence lengths for the Frenkel exciton states or indirectly by mixing of the Frenkel excitons with CT states.^{38,51,70} In either case, an increased delocalization would require the short-ranged intermolecular interactions of aggregates, and so the dilute TIPS-Pn:PMMA films (such as $F_2^{(B)}$ in Figure 6a) would not exhibit this effect (as schematically shown in Figure 7b(i)) and follow the observed reduced scaling relationship $2V_{0m} \propto \sqrt{f_{0m}}$.

4.3. Effect of Local Nanomorphology. The breaking of the scaling relationship for pristine TIPS-Pn films is made even more interesting when TIPS-Pn is compared with other (thio)acene-containing cavity systems, in particular diF TES-ADT and TIPS-Tc-based cavities used in our previous work.^{30,32} In the case of diF TES-ADT:PMMA films (discussed in our previous publication,³² cf. the data included in gray in Figure S13), cavities with mixed crystalline and

amorphous phases (the $P_{1.5}$ film, similar to the $F_1^{(B)}$ film here), showed the expected $2V_{om} \propto \sqrt{f_{om}}$ scaling relationship while coupling only to the amorphous phase, exactly the scenario observed for the $F_1^{(B)}$ TIPS-Pn:PMMA film. The slope obtained from linear fits of the data for diF TES-ADT:PMMA film $P_{1.5}$ in Figure S13a to eq 2 yielded 140 ± 10 meV. This is in between the slopes of 73 ± 10 and 222 ± 10 meV for $F_2^{(B)}$ and $F_1^{(B)}$ data in Figure 6a (Table S7), as expected based on the molecular densities in these films and the DFT-calculated oscillator strengths $f_{s_0-s_1}$ for the R-Pn and diF R-ADT molecules (Table S9). Furthermore, cavities containing highly concentrated crystalline diF TES-ADT:PMMA films (P_{agg} similar to the $F^{(P)}$ TIPS-Pn film here) exhibited a nearly constant $2V_{om}$ interaction strength (320 ± 8 meV, Figure S13a and Table S7),³² which is a behavior similar to $F^{(P)}$ cavity (which exhibited a nearly constant interaction strength of 210 ± 7 meV, Figure 6a and Table S7).

Interestingly, in contrast to pristine TIPS-Pn and highly concentrated diF TES-ADT:PMMA films, in pristine amorphous TIPS-Tc films the interaction strength $2V_{om}$ scaled well with the square root of the oscillator strength (f_{om}) (Figure S15) like the behavior of dilute TIPS-Pn:PMMA blends such as $F_2^{(B)}$.³⁰ This raises a question of the origin of the main differences between the TIPS-Tc and TIPS-Pn films and of similarity between TIPS-Pn and diF TES-ADT films which leads to such drastically different behavior of the interaction strengths in TIPS-Tc as compared to TIPS-Pn and diF TES-ADT. A distinguishing feature for TIPS-Tc as compared to TIPS-Pn and diF TES-ADT is that its molecular packing motif is conducive to forming π -stacked molecular pairs that are arranged in a herringbone geometry (one-dimensional (1D) sandwich-herringbone).⁷⁵ This is in contrast to TIPS-Pn and diF TES-ADT, both of which tend to form a more two-dimensional (2D) brickwork structure that may provide a denser set of molecules that increases the probability of delocalization.⁴³ We hypothesize that differences in local nanomorphology—driven by the differences in molecular packing motifs—are behind the differences in $2V_{om}$ scaling with the oscillator strength f_{om} in Figure 6a and Figure S15. In this case, even in the absence of the long-range order such as the case of TIPS-Pn amorphous films $A^{(P)}$ and TIPS-Tc amorphous films, the nanoaggregates that couple to the cavity retain molecular packing features similar to those derived from the crystal structure of these materials. For example, the TIPS-Tc molecules would tend to form relatively isolated π - π stacked dimer pairs (driven by 1D sandwich-herringbone packing tendency), whereas TIPS-Pn would tend to have a larger number of nearest neighbors (driven by 2D brickwork packing tendency). Then, the TIPS-Tc would be expected to exhibit a more localized exciton behavior as compared to TIPS-Pn. This would limit the effect of vibronic exciton delocalization (thus, leading to the scenario of Figure 7b(i) as compared to Figure 7b(ii)), discussed above for TIPS-Pn cavities, on the coupling strengths in TIPS-Tc films and lead to a similar scaling with the f_{om} oscillator strengths for both dilute blends and pristine films. Qualitatively similar observations of the molecular packing motif-induced differences in exciton delocalization have been previously made in single crystals of diF TSBS-ADT (1D sandwich-herringbone, conducive to localization) versus diF TES-ADT (2D brickwork, conducive to delocalization).³⁸ Such morphology-driven differences in localization on the molecular level sampled by the cavity

coupling of the vibronic excitons translate into the differences in the interaction strength scaling with the "apparent" oscillator strengths (obtained from optical absorption spectra of bare films) highlighting the ability of polariton spectroscopy to reveal not only hidden molecular populations but also their nanoscale-level morphologies.

5. CONCLUSION

In summary, we established how strong exciton–photon coupling evolves in TIPS-Pn-based films placed in all-metal cavities, depending on the molecular density and film morphology. The highest exciton–photon interaction strengths of up to ~ 270 meV were observed in pristine amorphous TIPS-Pn films, and the interaction strength for the lowest-energy (0–0) excited state scaled with the square root of the molecular density, independent of whether the long-range molecular order was present. The population most strongly coupled to the cavity was revealed to originate from the disordered regions in all films, including pristine crystalline films, with molecular configurations favorable for interacting with the cavity electric field. Such populations are not readily apparent from optical absorption spectra of bare films, which illustrates the capacity of polariton spectroscopy for revealing these hidden ensembles in heterogeneous (mixed-phase) and crystalline films. A breakdown of the scaling of the exciton–photon interaction strength with the square root of the oscillator strengths for the vibronic excitons, obtained from optical absorption spectra of bare films, was observed in pristine TIPS-Pn films. This observation was attributed to enhanced exciton delocalization of vibronic excitons that relies on short-range intermolecular interactions determined by the molecular packing motif, and in the case of TIPS-Pn, facilitated by the 2D brickwork motif of TIPS-Pn. Similar observations were made for diF TES-ADT films which share the same 2D brickwork packing motif conducive to delocalization, while differing from those in TIPS-Tc films hypothesized to favor a nanomorphology less conducive to delocalization (such as 1D sandwich-herringbone motif observed in crystalline TIPS-Tc).

Toward an overarching goal of utilizing the highly coherent nature of polariton states in boosting the performance of organic (opto)electronic devices based on benchmark organic semiconductors under study, our findings have important implications. In particular, since both charge carrier transport and singlet fission rely on the long-range molecular order for achieving best performance, the preferential cavity photon coupling to the molecular population in disordered regions has a potential to mitigate the negative impact of disorder on the device characteristics and relax the requirement of a highly ordered system, achieving enhanced electronic characteristics in disordered strongly coupled films instead. A study of a relatively dilute TIPS-Pn:polymer blend in a microcavity in ref 59 found only a weak effect of the exciton–photon coupling on the singlet fission. However, it would be interesting to examine more concentrated films and explore how the preferential cavity coupling to disordered populations in mixed-phase concentrated blends and crystals observed here would influence the dynamics of the entangled triplet pairs (TT). Tuning the molecular concentration in the strongly coupled model organic semiconductors such as TIPS-Pn also presents an opportunity to systematically investigate the effects of the interplay between the intermolecular interactions and coupling to the cavity photon on the singlet fission (e.g., ref 76) and photoinduced charge carrier dynamics.

■ ASSOCIATED CONTENT

SI Supporting Information

The Supporting Information is available free of charge at <https://pubs.acs.org/doi/10.1021/acs.jpcc.1c08257>.

Details of sample preparation, ellipsometry, and XRD characterization of films, optical spectra for various TIPS-Pn-based samples with fits, PL spectra and lifetimes, reflectance spectroscopy data for TIPS-Tc films in all-metal cavities with fits to the coupled oscillators model, fit parameters for various scaling characteristics of the coupling strengths in TIPS-Pn and diF TES-ADT films, DFT calculations for R-Pn, diF R-ADT, and R-Tc molecules (PDF)

■ AUTHOR INFORMATION

Corresponding Author

Oksana Ostroverkhova – Department of Physics, Oregon State University, Corvallis, Oregon 97331, United States;

orcid.org/0000-0002-3833-161X; Email: oksana@science.oregonstate.edu

Authors

Jonathan D. B. Van Schenck – Department of Physics, Oregon State University, Corvallis, Oregon 97331, United States

Winston T. Goldthwaite – Department of Physics, Oregon State University, Corvallis, Oregon 97331, United States

Richard Puro – Department of Physics, Oregon State University, Corvallis, Oregon 97331, United States

John E. Anthony – Center for Applied Energy Research, University of Kentucky, Lexington, Kentucky 40511, United States; orcid.org/0000-0002-8972-1888

Complete contact information is available at: <https://pubs.acs.org/10.1021/acs.jpcc.1c08257>

Notes

The authors declare no competing financial interest.

■ ACKNOWLEDGMENTS

We thank Prof. B. Gibbons and Dr. D. Fast for the access to the X-ray diffraction and ellipsometry facilities as well as N. Quist, R. Tollefsen, Dr. K. Tanyi, and Prof. L.-J. Cheng for helpful discussions. This work was supported by the National Science Foundation (NSF) (DMR-1808258 and CHE-1956431). The fabrication of microcavities was enabled by the NSF NNCI:NNI EECs-2025489 award. The synthesis of organic semiconductors was supported by the NSF under cooperative agreement No. 1849213.

■ ABBREVIATIONS

ADT = anthradithiophene; CT = charge transfer; GW/BSE = GW/Bethe–Salpeter equation; DFT = density functional theory; LP = lower polariton; PMMA = poly(methyl methacrylate); Pn = pentacene; Tc = tetracene; TES = triethylsilylethynyl; TIPS = triisopropylsilylethynyl.

■ REFERENCES

- (1) Ostroverkhova, O. Organic Optoelectronic Materials: Mechanisms and Applications. *Chem. Rev.* **2016**, *116*, 13279–13412.
- (2) Ostroverkhova, O., Ed.; *Handbook of Organic Materials for Electronic and Photonic Devices*, 2nd ed.; Woodhead Publishing: 2018.

- (3) Keeling, J.; Kena-Cohen, S. Bose–Einstein Condensation of Exciton-Polaritons in Organic Microcavities. *Annu. Rev. Phys. Chem.* **2020**, *71*, 435–459.

- (4) Ebbesen, T. W. Hybrid Light–Matter States in a Molecular and Material Science Perspective. *Acc. Chem. Res.* **2016**, *49*, 2403–2412.

- (5) Torma, P.; Barnes, W. L. Strong Coupling Between Surface Plasmon Polaritons and Emitters: a Review. *Rep. Prog. Phys.* **2015**, *78*, 013901.

- (6) Tanyi, K.; Hong, N.; Sawyer, T.; Van Schenck, J.; Giesbers, G.; Ostroverkhova, O.; Cheng, L. J. Strong exciton-plasmon coupling in dye-doped film on a planar hyperbolic metamaterial. *Opt. Lett.* **2020**, *45*, 6736.

- (7) Spano, F. Optical microcavities enhance the exciton coherence length and eliminate vibronic coupling in J-aggregates. *J. Chem. Phys.* **2015**, *142*, 184707.

- (8) Spano, F. Exciton–phonon polaritons in organic microcavities: Testing a simple ansatz for treating a large number of chromophores. *J. Chem. Phys.* **2020**, *152*, 204113.

- (9) Herrera, F.; Owrutsky, J. Molecular polaritons for controlling chemistry with quantum optics. *J. Chem. Phys.* **2020**, *152*, 100902.

- (10) Ribeiro, R. F.; Martínez-Martínez, L. A.; Du, M.; Campos-Gonzalez-Angulo, J.; Yuen-Zhou, J. Polariton chemistry: controlling molecular dynamics with optical cavities. *Chemical Science* **2018**, *9*, 6325–6339.

- (11) Wei, M.; Rajendran, S. K.; Ohadi, H.; Tropf, L.; Gather, M. C.; Turnbull, G. A.; Samuel, I. D. W. Low-threshold polariton lasing in a highly disordered conjugated polymer. *Optica* **2019**, *6*, 1124–1129.

- (12) Putintsev, A.; Zasedatelev, A.; McGhee, K. E.; Cookson, T.; Georgiou, K.; Sannikov, D.; Lidzey, D. G.; Lagoudakis, P. G. Nano-second exciton-polariton lasing in organic microcavities. *Appl. Phys. Lett.* **2020**, *117*, 123302.

- (13) Kena-Cohen, S.; Forrest, S. Room-temperature polariton lasing in an organic single-crystal microcavity. *Nat. Photonics* **2010**, *4*, 371–375.

- (14) Zasedatelev, A.; Baranikov, A.; Urbonas, D.; Scafirimuto, F.; Scherf, U.; Stoferle, T.; Mahrt, R.; Lagoudakis, P. G. A room-temperature organic polariton transistor. *Nat. Photonics* **2019**, *13*, 378–383.

- (15) Lerario, G.; Fieramosca, A.; Barachati, F.; Ballarini, D.; Daskalakis, K.; Dominici, L.; De Giorgi, M.; Maier, S.; Gigli, G.; Kena-Cohen, S.; et al. Room-temperature superfluidity in a polariton condensate. *Nat. Phys.* **2017**, *13*, 837–841.

- (16) Gubbin, C.; Maier, S.; Kena-Cohen, S. Low-voltage polariton electroluminescence from an ultrastrongly coupled organic light-emitting diode. *Appl. Phys. Lett.* **2014**, *104*, 233302.

- (17) Eizner, E.; Brodeur, J.; Barachati, F.; Sridharan, A.; Kena-Cohen, S. Organic Photodiodes with an Extended Responsivity using Ultrastrong Light-Matter Coupling. *ACS Photonics* **2018**, *5*, 2921–2927.

- (18) Krainova, N.; Grede, A. J.; Tsokkou, D.; Banerji, N.; Giebink, N. C. Polaron Photoconductivity in the Weak and Strong Light-Matter Coupling Regime. *Phys. Rev. Lett.* **2020**, *124*, 177401.

- (19) Wang, M.; Hertzog, M.; Borjesson, K. Polariton-assisted excitation energy channeling in organic heterojunctions. *Nat. Commun.* **2021**, *12*, 1874.

- (20) Nikolis, V. C.; Mischok, A.; Siegmund, B.; Kublitski, J.; Jia, X.; Benduhn, J.; Hormann, U.; Neher, D.; Gather, M. C.; Spoltore, D.; Vandewal, K. Strong light-matter coupling for reduced photon energy losses in organic photovoltaics. *Nat. Commun.* **2019**, *10*, 3706.

- (21) Orgiu, E.; George, J.; Hutchison, J.; Devaux, E.; Dayen, J.; Doudin, B.; Stellacci, F.; Genet, C.; Schachenmayer, J.; Genes, C.; et al. Conductivity in organic semiconductors hybridized with the vacuum field. *Nat. Mater.* **2015**, *14*, 1123–1129.

- (22) Kang, E.; Chen, S.; Derek, V.; Hagglund, C.; Glowacki, E. D.; Jonsson, M. P. Charge transport in phthalocyanine thin-film transistors coupled with Fabry–Perot cavities. *J. Mater. Chem. C* **2021**, *9*, 2368–2374.

- (23) Held, M.; Graf, A.; Zakharko, Y.; Chao, P.; Tropf, L.; Gather, M.; Zaumseil, J. Ultrastrong Coupling of Electrically Pumped Near-

Infrared Exciton-Polaritons in High Mobility Polymers. *Adv. Opt. Mater.* **2018**, *6*, 1700962.

(24) Coles, D.; Somaschi, N.; Michetti, P.; Clark, C.; Lagoudakis, P.; Savvidis, P.; Lidzey, D. G. Polariton-mediated energy transfer between organic dyes in a strongly coupled optical microcavity. *Nat. Mater.* **2014**, *13*, 712–719.

(25) Liu, B.; Rai, P.; Grezma, J.; Twieg, R. J.; Singer, K. D. Coupling of exciton-polaritons in low-Q coupled microcavities beyond the rotating wave approximation. *Phys. Rev. B: Condens. Matter Mater. Phys.* **2015**, *92*, 155301.

(26) Cheng, C.; Kim, N.; Giebink, N. Charged Polariton Luminescence from an Organic Semiconductor Microcavity. *ACS Photonics* **2019**, *6*, 308–313.

(27) Sliotzky, M.; Zhang, Y.; Forrest, S. R. Temperature dependence of polariton lasing in a crystalline anthracene microcavity. *Phys. Rev. B: Condens. Matter Mater. Phys.* **2012**, *86*, 045312.

(28) Polak, D.; Jayaprakash, R.; Lyons, T. P.; Martínez-Martínez, L. A.; Leventis, A.; Fallon, K. J.; Coulthard, H.; Bossanyi, D. G.; Georgiou, K.; Petty, A. J.; et al. Manipulating molecules with strong coupling: harvesting triplet excitons in organic exciton microcavities. *Chem. Sci.* **2020**, *11*, 343–354.

(29) Kena-Cohen, S.; Forrest, S. R. Giant Davydov splitting of the lower polariton branch in a polycrystalline tetracene microcavity. *Phys. Rev. B: Condens. Matter Mater. Phys.* **2008**, *77*, 073205.

(30) Puro, R.; Van Schenck, J. D. B.; Center, R.; Holland, E.; Anthony, J. E.; Ostroverkhova, O. Exciton polariton-enhanced photodimerization of functionalized tetracene. *J. Phys. Chem. C* **2021**, DOI: 10.1021/acs.jpcc.1c06881.

(31) Liu, B.; Menon, V.; Sfeir, M. Ultrafast thermal modification of strong coupling in an organic microcavity. *APL Photonics* **2021**, *6*, 016103.

(32) Van Schenck, J.; Tanyi, E. K.; Cheng, L.-J.; Anthony, J.; Ostroverkhova, O. Strong exciton-photon coupling in anthradithiophene microcavities: from isolated molecules to aggregates. *MRS Commun.* **2019**, *9* (3), 956–963.

(33) Moerner, W. E.; Kador, L. Optical detection and spectroscopy of single molecules in a solid. *Phys. Rev. Lett.* **1989**, *62*, 2535.

(34) Ambrose, W. P.; Basche, T.; Moerner, W. E. Detection and spectroscopy of single pentacene molecules in a p-terphenyl crystal by means of fluorescence excitation. *J. Chem. Phys.* **1991**, *95*, 7150.

(35) Orrit, M.; Bernard, J. Single pentacene molecules detected by fluorescence excitation in a p-terphenyl crystal. *Phys. Rev. Lett.* **1990**, *65*, 2716.

(36) Shepherd, W. E. B.; Grollman, R.; Robertson, A.; Paudel, K.; Hallani, R.; Loth, M. A.; Anthony, J. E.; Ostroverkhova, O. Single-molecule imaging of organic semiconductors: Toward nanoscale insights into photophysics and molecular packing. *Chem. Phys. Lett.* **2015**, *629*, 29–35.

(37) Grollman, R.; Quist, N.; Robertson, A.; Rath, J.; Purushothaman, B.; Haley, M. M.; Anthony, J. E.; Ostroverkhova, O. Single-molecule insight into nanoscale environment-dependent photophysics in blends. *J. Phys. Chem. C* **2017**, *121*, 12483–12494.

(38) Van Schenck, J.; Mayonado, G.; Anthony, J.; Graham, M.; Ostroverkhova, O. Molecular packing-dependent exciton dynamics in functionalized anthradithiophene derivatives: from solutions to crystals. *J. Chem. Phys.* **2020**, *153*, 164715.

(39) Ostroverkhova, O.; Cooke, D. G.; Hegmann, F. A.; Anthony, J. E.; Podzorov, V.; Gershenson, M. E.; Jurchescu, O. D.; Palstra, T. T. M. Ultrafast carrier dynamics in pentacene, functionalized pentacene, tetracene, and rubrene single crystals. *Appl. Phys. Lett.* **2006**, *88*, 162101.

(40) Hestand, N.; Yamagata, H.; Xu, B.; Sun, D.; Zhong, Y.; Harutyunyan, A.; Chen, G.; Dai, H.; Rao, Y.; Spano, F. C. Polarized Absorption in Crystalline Pentacene: Theory vs Experiment. *J. Phys. Chem. C* **2015**, *119*, 22137–22147.

(41) Cruz, C.; Chronister, E.; Bardeen, C. J. Using temperature dependent fluorescence to evaluate singlet fission pathways in tetracene single crystals. *J. Chem. Phys.* **2020**, *153*, 234504.

(42) Johnson, J. Open questions on the photophysics of ultrafast singlet fission. *Commun. Chem.* **2021**, *4*, 85.

(43) Anthony, J. E. The Larger Acenes: Versatile Organic Semiconductors. *Angew. Chem., Int. Ed.* **2008**, *47*, 452–483.

(44) Diao, Y.; Lenn, K.; Lee, W.; Blood-Forsythe, M.; Xu, J.; Mao, Y.; Kim, Y.; Reinspach, J. A.; Park, S.; Aspuru-Guzik, A.; et al. Understanding Polymorphism in Organic Semiconductor Thin Films through Nanoconfinement. *J. Am. Chem. Soc.* **2014**, *136*, 17046–17057.

(45) Ostroverkhova, O.; Cooke, D. G.; Shcherbina, S.; Egerton, R.; Tykwinski, R. R.; Anthony, J. E.; Hegmann, F. A. Band-like transport in pentacene and functionalized pentacene thin films revealed by sub-picosecond transient photoconductivity measurements. *Phys. Rev. B: Condens. Matter Mater. Phys.* **2005**, *71*, 035204.

(46) Giri, G.; Park, S.; Vosgueritchian, M.; Shulaker, M.; Bao, Z. High-Mobility, Aligned Crystalline Domains of TIPS-Pentacene with Metastable Polymorphs Through Lateral Confinement of Crystal Growth. *Adv. Mater.* **2014**, *26*, 487–493.

(47) Knepp, D.; Talnack, F.; Boroujeni, B. K.; Teixeira da Rocha, C.; Höppner, M.; Tahn, A.; Mannsfeld, S. C. B.; Ellinger, F.; Leo, K.; Kleemann, H. Solution-processed pseudo-vertical organic transistors based on TIPS-pentacene. *Materials Today Energy* **2021**, *21*, 100697.

(48) Ostroverkhova, O.; Shcherbina, S.; Cooke, D.; Egerton, R.; Hegmann, F.; et al. Optical and transient photoconductive properties of pentacene and functionalized pentacene thin films: Dependence on film morphology. *J. Appl. Phys.* **2005**, *98*, 033701.

(49) Anthony, J. E.; Brooks, J. S.; Eaton, D. L.; Parkin, S. R. Functionalized Pentacene: Improved Electronic Properties from Control of Solid-State Order. *J. Am. Chem. Soc.* **2001**, *123* (38), 9482–9483.

(50) Jones, A.; Kearns, N.; Ho, J.; Flach, J.; Zanni, M. Impact of non-equilibrium molecular packings on singlet fission in microcrystals observed using 2D white-light microscopy. *Nat. Chem.* **2020**, *12*, 40–47.

(51) Wong, C.; Cotts, B.; Wu, H.; Ginsberg, N. Exciton dynamics reveal aggregates with intermolecular order at hidden interfaces in solution-cast organic semiconducting films. *Nat. Commun.* **2015**, *6*, 5946.

(52) Munson, K. T.; Gan, J.; Grieco, C.; Doucette, G. S.; Anthony, J. E.; Asbury, J. B. Ultrafast Triplet Pair Separation and Triplet Trapping following Singlet Fission in Amorphous Pentacene Films. *J. Phys. Chem. C* **2020**, *124* (43), 23567–23578.

(53) Grieco, C.; Doucette, G. S.; Pensack, R. D.; Payne, M. M.; Rimshaw, A.; Scholes, G. D.; Anthony, J. E.; Asbury, J. B. Dynamic Exchange During Triplet Transport in Nanocrystalline TIPS-Pentacene Films. *J. Am. Chem. Soc.* **2016**, *138*, 16069–16080.

(54) Walker, B.; Musser, A.; Beljonne, D.; Friend, R. H. Singlet exciton fission in solution. *Nat. Chem.* **2013**, *5*, 1019–1024.

(55) Grieco, C.; Doucette, G. S.; Munson, K. T.; Swartzfager, J. R.; Munro, J. M.; Anthony, J. E.; Dabo, I.; Asbury, J. B. Vibrational probe of the origin of singlet exciton fission in TIPS-pentacene solutions. *J. Chem. Phys.* **2019**, *151*, 154701.

(56) Sharifzadeh, S.; Wong, C.; Wu, H.; Cotts, B.; Kronik, L.; Ginsberg, N.; Neaton, J. B. Relating the Physical Structure and Optoelectronic Function of Crystalline TIPS-Pentacene. *Adv. Funct. Mater.* **2015**, *25*, 2038–2046.

(57) Pensack, R. D.; Grieco, C.; Purdum, G. E.; Mazza, S. M.; Tilley, A. J.; Ostroumov, E. E.; Seferos, D. S.; Loo, Y.-L.; Asbury, J. B.; Anthony, J. E.; et al. Solution-processable, crystalline material for quantitative singlet fission. *Mater. Horiz.* **2017**, *4*, 915.

(58) Yang, L.; Tabachnyk, M.; Bayliss, S. L.; Böhm, M. L.; Broch, K.; Greenham, N. C.; Friend, R. H.; Ehrler, B. Solution-Processable Singlet Fission Photovoltaic Devices. *Nano Lett.* **2015**, *15*, 354–358.

(59) Liu, B.; Menon, V.; Sfeir, M. The Role of Long-Lived Excitons in the Dynamics of Strongly Coupled Molecular Polaritons. *ACS Photonics* **2020**, *7*, 2292–2301.

(60) Moerner, W. E.; Orrit, M. Illuminating Single Molecules in Condensed Matter. *Science* **1999**, *283*, 1670–1676.

(61) Shepherd, W.; Platt, A.; Hofer, D.; Ostroverkhova, O.; Loth, M.; Anthony, J. Aggregate formation and its effect on (opto)-electronic properties of guest-host organic semiconductors. *Appl. Phys. Lett.* **2010**, *97*, 163303.

(62) Paudel, K.; Giesbers, G.; Van Schenck, J.; Anthony, J. E.; Ostroverkhova, O. Molecular packing-dependent photoconductivity in functionalized anthradithiophene crystals. *Org. Electron.* **2019**, *67*, 311–319.

(63) Fox, M. *Quantum Optics: An Introduction*; Oxford University Press: 2005.

(64) Arago, J.; Viruela, P. M.; Orti, E.; Osuna, R.; Hernandez, V.; Lopez Navarrete, J. T.; Swartz, C. R.; Anthony, J. E. Functionalized pentacenes: a combined theoretical, Raman and UV–Vis spectroscopic study. *Theor. Chem. Acc.* **2011**, *128*, 521–530.

(65) Xu, J.; Diao, Y.; Zhou, D.; Mao, Y.; Giri, G.; Chen, W.; Liu, N.; Mannsfeld, S. C. B.; Xue, G.; Bao, Z. Probing the interfacial molecular packing in TIPS-pentacene organic semiconductors by surface enhanced Raman scattering. *J. Mater. Chem. C* **2014**, *2*, 2985.

(66) Le, D. V.; de la Perrelle, J. M.; Do, T. N.; Leng, X.; Tapping, P. C.; Scholes, G. D.; Kee, T. W.; Tan, H.-S. Characterization of the ultrafast spectral diffusion and vibronic coherence of TIPS-pentacene using 2D electronic spectroscopy. *J. Chem. Phys.* **2021**, *155*, 014302.

(67) Ohno, K. Simple calculations of Franck-Condon factors for electronic transition bands of polyacenes. *Chem. Phys. Lett.* **1978**, *53*, 571–577.

(68) Yamagata, H.; Maxwell, D.; Fan, J.; Kittilstved, K.; Briseno, A.; Barnes, M.; Spano, F. C. *J. Phys. Chem. C* **2014**, *118*, 28842.

(69) James, D.; Frost, J.; Wade, J.; Nelson, J.; Kim, J. Controlling Microstructure of Pentacene Derivatives by Solution Processing: Impact of Structural Anisotropy on Optoelectronic Properties. *ACS Nano* **2013**, *7*, 7983–7991.

(70) Li, Y.; Wan, J.; Smilgies, D.; Miller, R.; Headrick, R. Enhancement of charge transfer in thermally-expanded and strain-stabilized TIPS-pentacene thin films. *Phys. Rev. Res.* **2020**, *2*, 033294.

(71) Hestand, N.; Spano, F. C. Expanded Theory of H- and J-Molecular Aggregates: The Effects of Vibronic Coupling and Intermolecular Charge Transfer. *Chem. Rev.* **2018**, *118*, 7069–7163.

(72) Litinskaya, M.; Reineker, P. Loss of coherence of exciton polaritons in inhomogeneous organic microcavities. *Phys. Rev. B: Condens. Matter Mater. Phys.* **2006**, *74*, 165320.

(73) Le Roux, F.; Bradley, D. D. C. Conformational control of exciton-polariton physics in metal-poly(9,9-dioctylfluorene)-metal cavities. *Phys. Rev. B: Condens. Matter Mater. Phys.* **2018**, *98*, 195306.

(74) Van Schenck, J. D. B. Exciton and Polariton Nature in Organic Crystals. Ph.D. Thesis, Oregon State University, 2021.

(75) Stern, H.; Cheminal, A.; Yost, S. R.; Broch, K.; Bayliss, S.; Chen, K.; Tabachnyk, M.; Thorley, K.; Greenham, N.; Hodgkiss, J.; et al. Vibronically coherent ultrafast triplet-pair formation and subsequent thermally activated dissociation control efficient endothermic singlet fission. *Nat. Chem.* **2017**, *9*, 1205–1212.

(76) Zhang, B.; Zhao, Y.; Liang, W. Z. Joint Effects of Exciton-Exciton and Exciton-Photon Couplings on the Singlet Fission Dynamics in Organic Aggregates. *J. Phys. Chem. C* **2021**, *125*, 1654–1664.